Geophysical Journal International

Geophys. J. Int. (2013) **194,** 1955–1965
Advance Access publication 2013 June 18

doi: 10.1093/gji/ggt214

Three-dimensional passive imaging of complex seismic fault systems: evidence of surface traces of the Issyk-Ata fault (Kyrgyzstan)

Marco Pilz, Stefano Parolai and Dino Bindi
Helmholtz Center Potsdam – GFZ German Research Center for Geosciences, Helmholtzstr. 7, 14467 Potsdam, Germany. E-mail: pilz@gfz-potsdam.de

Accepted 2013 May 21. Received 2013 March 19; in original form 2013 January 24

SUMMARY

Nowadays, an increasing number of seismological imaging studies are published taking advantage of the increasing popularity of analysing empirical Green's functions obtained from high-frequency ambient seismic noise. However, especially on a local scale results could potentially be biased in regions where topography is not small compared to the wavelength and the penetration depth of the considered waves. Current 2-D seismic techniques are often inadequate when solving such 3-D geophysical problems, which include the complication of seismic imaging for cases where there are pronounced relief effects. For example, information about the geologic subsurface structure and deformational patterns is necessary for accurate site characterization and seismic hazard assessment. Here we show that an *ad hoc* passive seismic tomography approach can identify and describe complex 3-D structures, which can help to accurately and efficiently map the shear-wave velocities of the surficial soil layers, even in cases of significant topography relief. We test our technique by using simulations of seismic noise for a simple realistic site and show for a real data set across the Issyk-Ata fault, Kyrgyzstan, which is located at southern border of the capital, Bishkek, this novel approach has identified two different small fault branches and a clear shear-wave velocity contrast across the fault.

Key words: Interferometry; Surface waves and free oscillations; Seismic tomography; Fractures and faults.

1 INTRODUCTION

Characterization of the internal structure of fault zones is an essential prerequisite for understanding and predicting their mechanical and seismic properties. Large-displacement faults generally produce much wider zones of deformation than smaller offset features. This provides much more scope for developing a complex internal geometry, which in turn may lead to significant modifications of the properties of these discontinuities. For large fault zones, geological studies show that the principal fault slip zone is often localized along bimaterial interfaces that separate rock units with considerably different properties (Sengor *et al.* 2005; Dor *et al.* 2008; Mitchell *et al.* 2011). Sharp velocity contrasts are likely to be observed across major faults, which are generally interpreted as lithological discontinuities (Michelini & McEvilly 1991; Amato *et al.* 1992; Eberhart-Phillips & Michael 1993; O'Connell *et al.* 2007). Notably, a lithology contrast in the earthquake source region can produce an ambiguity in inferred seismic moments, associated with the multiple available choices for the assumed rigidity (Ben-Zion 1989; Heaton & Heaton 1989). Ben-Zion & Shi (2005) suggested, based on simulations of dynamic ruptures with off-fault plastic yielding, that strongly asymmetric damage zones on opposing sides of a fault are the cumulative product of earthquake ruptures on bimaterial faults separating different elastic bodies. Ignoring the near-surface structural properties across a seismic fault can produce biases and errors in derived earthquake locations and other structural properties and distort seismic hazard assessment (McNally & McEvilly 1977; Oppenheimer *et al.* 1988; Ben-Zion & Malin 1991).

The topic of active fault studies is not new: Since the pioneering work of Aki & Lee (1976) large scale 3-D imaging of the seismogenic upper crust has become an important tool for the investigation of the nature of active fault zones. The occurrence of the 1995 Great Hanshin earthquake exactly on the mapped Nojima Fault reconfirmed this idea, emphasizing the importance of active fault studies. Thus, precise mapping and imaging has become one of the key aspects in terms of the possible location of future surface ruptures and near-fault seismic hazard assessment. Over the last few years, our ability to identify active faults has improved significantly, but in the absence of drilling, surface-based geophysical methods are necessary for the proper identification of fault zones and for the exact characterization of their properties.

Nowadays, multiple observations of geophysical properties like seismic body wave velocities in and adjacent to fault zones offer the greatest hope of making inferences about the fault, but up to now their resolution has been limited, particularly precluding the imaging of small-scale near-surface features. Active seismic imaging profiles (refraction or wide-angle profiles) can be useful for imaging surficial subsurface structures with shallow dips such as low-angle faults (Mooney 1989); although, in contrast, vertical or almost vertical faults are difficult to be identified by such methods (Mooney & Brocher 1987).

Here we present a rapid procedure for the passive imaging of near-surface properties by a weighted 3-D inversion procedure that also works in case of complex 3-D *S*-wave velocity structures under pronounced topographic conditions. The presented method can offer a more comprehensive view of the subsurface, having a greater areal extent and greater depth than traditional methods such as trenching or drilling. The success of these passive applications is explained by the fact that these methods are based on surface waves, which are always present in the ambient seismic noise wave field because they are excited preferentially by superficial sources. These waves can easily be extracted because they dominate the Green's function between receivers located at the surface.

To extract the exact Green's function, perfect diffuseness of the illuminating field is required. However, the diffuseness of a field relies on the equipartition of energy, which corresponds to equal energies with the independent modes of vibration. In this case, the energies undergo conspicuous fluctuations as a function of depth within about one Rayleigh wavelength (Sánchez-Sesma *et al.* 2008; Perton *et al.* 2009). Statistical treatment can be applied to such random wavefields, in particular to long time-series of ambient seismic noise. Since the distribution of the ambient sources randomizes when averaged over longer times (not more than a few hours for frequencies higher than a few hertz) the stabilization of the normalized averaged correlation function suggests that the resulting illumination is totally or partially equipartitioned (Sánchez-Sesma *et al.* 2011).

Important developments in methodology set this work apart from previous studies: The estimated traveltimes were inverted by a rapid one-step tomographic algorithm. We decided in favour of this approach to calculate a 3-D *S*-wave velocity model instantaneously, keeping in mind a future application to monitoring. Moreover, classical imaging techniques are based on a flat Earth surface, implicitly assuming that the waves travel perfectly horizontally and do not follow the topography. Although this approximation is likely to be true for small frequency waves with wavelengths much greater than the amplitude of topographic variations due to the rather small penetration depths and short wavelengths of anthropogenic ambient seismic noise, in the case of strong topographic relief, a failure to use the right path length between the individual stations will lead to strong biases towards too small velocities (Wang *et al.* 2012). This emphasizes the necessity that the inversion algorithm must properly account for the effects of topography.

Hereunto, we will first give an outline of the calculation of Rayleigh wave phase velocities and a description of the 3-D inversion procedure. To validate the technique, a synthetic example is presented, including a detailed discussion on the resolution of the algorithm and on some of the problems that can be encountered in tomographic inversion. Finally, after describing the data collection for a real-world data set on the Issyk-Ata fault in Kyrgyzstan, we will show that this approach can identify near-surface features across this fault.

2 CALCULATION OF TRAVELTIMES

The calculation of the Rayleigh wave phase velocities is based on the frequency-domain SPAC technique of Aki (1957). Whereas the classical SPAC method is used to retrieve the shallow *S*-wave velocity structure below a small array by means of the inversion of surface wave dispersion curves and, therefore, assumes an (almost) 1-D velocity–depth profile it is clear that for non-homogeneous subsoil conditions, the method suffers a severe drawback. That is, if the situation is more complicated (as, for example, across a region with a large velocity contrast) the classical SPAC method will provide significant perturbations in the observed *S*-wave velocity structure (Foti *et al.* 2011). On the other hand, one can expect that, similarly to what is obtained over regional scales, local heterogeneities will affect the noise propagation on a small scale along the ray path between the sensors, and hence can be retrieved by analysing the Green's function estimated by the cross-correlation of the signals recorded at two different stations (Brenguier *et al.* 2007; Picozzi *et al.* 2009). As shown by Tsai & Moschetti (2010), the exact equivalence between the cross-correlation and the SPAC allows the results from each of the independent fields to be used in the other.

As discussed in Ohori *et al.* (2002), if the microtremor wavefield is stochastic and stationary in both space and time, the azimuthally averaged correlation function for one angular frequency ω_0 can be expressed in the form

$$\rho\,(r,\omega_0) = J_0\left[\frac{\omega_0}{c\,(\omega_0)}r\right], \tag{1}$$

where $c(\omega_0)$ is the frequency-dependent phase velocity, r is the interstation distance and J_0 is the zero order Bessel function. Considering that experimental values of the azimuthally averaged spatial correlation function $\rho\,(r,\omega_0)$ can be obtained from seismic noise measurements carried out with 2-D arrays of seismic stations, by fitting these latter values to the theoretical Bessel function values, the phase velocity $c(\omega_0)$ can be retrieved by equating the zero crossings of the real part of the spectrum with the zero crossings of the Bessel function (Ekström *et al.* 2009). Although the amplitude of the real part of the spectrum depends on the background noise spectrum, the locations of the zero crossings in the spectrum are insensitive to variations in the spectral power of the background noise.

For calculating the cross-correlation functions between the stations, we consider only the vertical component of the recordings, which are strongly dominated by Rayleigh waves. A second order Butterworth high-pass filter was applied to these data using a corner frequency of 0.9 Hz, aiming at removing high-amplitude low-frequency irregularities that tend to obscure noise signals. For each of the chosen frequencies and for all $n(n-1)/2$ possible station pairs, where n is the number of stations, the data were one-bit normalized (Campillo & Paul 2003) and, finally, stacked together which, on average, improves the signal-to-noise ratio. Finally, the traveltimes between all stations were calculated from the estimated phase velocities using the known distances between the sensors.

3 THE INVERSION ALGORITHM

The estimated traveltimes for the individual frequencies were inverted by a rapid tomographic algorithm to calculate a 3-D *S*-wave velocity model similar to Pilz *et al.* (2012) but accounting for the topographic relief. Since the *S*-wave velocity is the dominant property of the fundamental mode of high-frequency Rayleigh waves, we perform inversions for a *S*-wave velocity model estimation while considering the observed velocities in the 3-D frequency-dependent tomography as being representative of Rayleigh wave phase velocities.

Although the ray path is velocity dependent, meaning that traveltime inversion is a non-linear problem, deviations of the paths from a straight line will be less than a quarter of the wavelength. Hence, keeping in mind that there is also a small level of error for the input data for shallow seismic surveys (Kugler *et al.* 2007), we are sure that a bias of a few percent can be tolerated to keep the solution linear. Therefore, the propagation paths are assumed to be straight rays and the medium can be subdivided into a reasonable number of smaller cells, meaning that the problem can be expressed in a simple discrete matrix form to be used in practical applications

$$\mathbf{t} = \mathbf{L}_1 s. \tag{2}$$

$\mathbf{L}_1$ is an $RF \times MN$ matrix with R being the number of rays for F different frequencies crossing the medium that is subdivided into M cells in each of the N horizontal layers. The vector $\mathbf{t}$ corresponds to the traveltimes between each pair of receivers with a frequency dependent slowness s (inverse velocity).

Starting from a homogeneous 3-D velocity model, an iterative procedure using singular value decomposition for minimizing the misfit between the observed and theoretical traveltimes is adopted (Picozzi *et al.* 2009; Pilz *et al.* 2012). Additionally, to reduce the risk of divergence and to stabilize the iteration process, an adaptive bi-weight estimation (Tukey 1974; Arai & Tokimatsu 2004), which is a type of maximum likelihood estimation, is applied.

In particular, the measured slowness along each ray path contains information about the underlying structure to depths corresponding to approximately one-third to one-half the wavelength of each frequency (Foti *et al.* 2009). Since shallow blocks are sampled more intensely than deeper ones, we introduce a further constraint on the solution by adding a $MNF \times MNF$ weighting matrix $\mathbf{K}$ which weights the data depending on the number, length, orientation and vertical penetration depth of each ray path segment crossing each cell. According to Yanovskaya & Ditmar (1990), for the 3-D problem the weights in $\mathbf{K}$ turn out to be representable as a product of two functions, one depending on the horizontal properties, that is, the number, path length (in consideration of the relief, see explanation in the next paragraph) and orientation of the ray paths, and the other one depending on the vertical penetration depth, that is, the frequency of each ray path segment crossing each cell. Additional smoothness constraints are implemented by adding a system of equations to the original traveltime inversion problem, following Ammon & Vidale (1993) and Picozzi *et al.* (2009). Due to the rather small penetration depths and short wavelengths of ambient seismic noise, in the case of strong topographic relief, a failure to use the right path length in each of the cells will lead to incorrect weighting and therefore to biases towards too small velocities.

4 WEIGHTING SCHEME

For the horizontal weights, the singular values of the ray density matrix were used to calculate its ellipticity following Kissling (1988). If several rays with different azimuths cross the cell, the ellipticity is close to 1 and a good resolution for the cell is achieved. Therefore, the horizontal weights were computed by multiplying the ellipticity for the number of rays crossing each cell.

For quantifying the vertical penetration depth, the weights are calculated taking into account the different penetration depths of the individual frequencies and the slope of the topography. The weights are based on the analytical solution of displacement components for Rayleigh waves in a half space (Aki & Richards 1980)

$$u_3\left(|\mathbf{z}|\right) = \mathrm{l}e^{\mathrm{l}k\mathbf{z}\cdot\mathbf{e}_z} - \mathrm{s}e^{\mathrm{p}k\mathbf{z}\cdot\mathbf{e}_z} \tag{3}$$

with $\mathbf{z} \cdot \mathbf{e}_z = |z| \cos(\alpha)$ being the scalar product of the vector $\mathbf{z}$, measured perpendicular to the surface of the cell, and the unit vector $\mathbf{e}_z$, where α is the slope of surface topography for each of the cell columns (Fig. 1). For the entire surface of the block we define $|\mathbf{z}| := 0$. Please note that the scheme can account for different values for α for different parts of the block. $k = \omega_0/c_R$ is the Rayleigh wave number with c_R being the Rayleigh wave phase velocity and ω_0 being the angular frequency.

For our model, the Rayleigh wave velocity is assumed to be around 0.92 v_s, which is realistic for a multilayer model with typical values of Poisson's ratio ($0.2 < \upsilon < 0.4$; Xia *et al.* 1999). For the remaining parameters in eq. (3), this leads to $l = 0.8475$, $p = 0.3933$ and $s = 1.4679$ (Bullen 1963; Lay & Wallace 1995). The

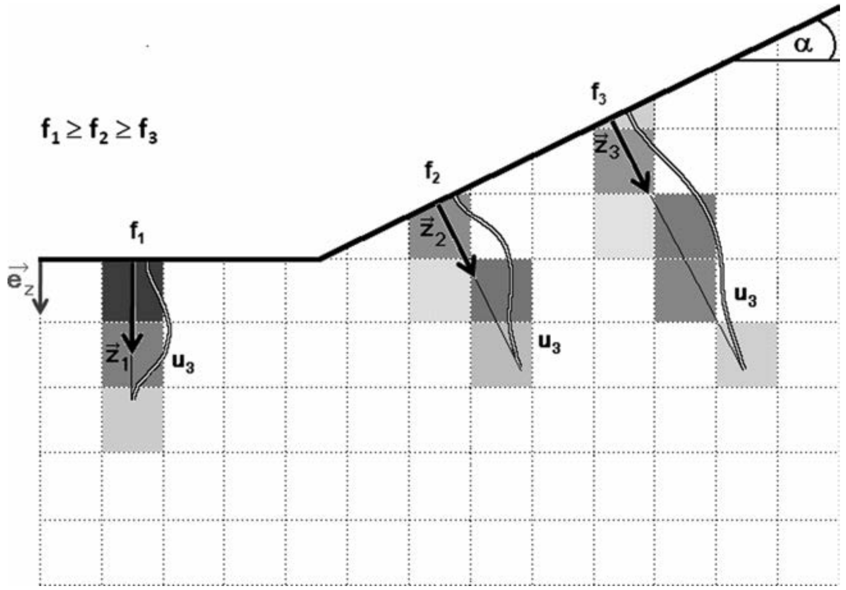

Figure 1. Calculation of the vertical weights for different frequencies for the block's cells, based on the displacement component u_3 for Rayleigh waves. The darker the individual cell's colour, the higher the weight. Note that the weight is calculated perpendicular to the slope of topography.

corresponding vertical weights w for the different frequencies are calculated as the normalized average values of u_3 for each cell,

$$w = \frac{\int_{r_1}^{r_2} u_3\,(z)\,\mathrm{d}z}{\int_{0}^{\infty} u_3\,(z)\,\mathrm{d}z}, \tag{4}$$

where r_1 and r_2 being the bounds at which u_3 is crossing the cell limits, respectively (see Fig. 1). In the case where no rays are crossing the cell, the weight is equal to zero. Since eqs (3) and (4) strongly depend on the underlying Rayleigh wave phase velocities, the weights for all cells, and accordingly the velocity vectors, are updated after each iteration step until a reasonable compromise between the reduction of the rms error between the observations and the predictions and the norm of the solution is reached. The updated slowness s is used to calculate the 3-D S-wave velocity v_s by $v_s = (0.92s)^{-1}$. The entire inversion procedure is run four times with a lateral shift of the grid to avoid a too-strong and misleading dependence on the chosen parametrization. In each run, the grid is shifted by half the cell size in both x and y direction, respectively, and the final S-wave velocity model is calculated as the average of the four samples (Cattaneo & Eva 1990; Evans & Achauer 1993).

5 SYNTHETIC TESTS

To ensure the reliability of the proposed technique, synthetic time-series of seismic noise were computed using a spectral element code, developed by the Center for Advanced Studies, Research and Development, in Sardinia and the Department of Structural Engineering of the Politecnico di Milano (Faccioli *et al.* 1997). The underlying model consists of a block with two homogeneous layers characterized by different S-wave velocities with the intersecting plane of the two structures dipping at an angle of around 50°. The surface of the modelled block is characterized by a gradient with the slope angle changing where the two blocks emerge at the surface (Fig. 2). There is a shift of the velocity contrast towards the bottom of the slope at 18 m below the surface of the low-velocity block. Since only cultural noise higher than a few Hertz is considered, such synthetic wave fields can be modelled as a distribution of impulsive point forces located at the surface or subsurface of the studied medium, having random force orientation and amplitude (Lachet & Bard 1994). Such a random force was applied at each time step of 0.01 s at 200 different locations, arbitrarily distributed over an area covering the entire block's surface and a frame being 100 meters wide and surrounding the block. The noise sources are distributed isotropically around the area of interest guaranteeing a diffuse noise wave field.

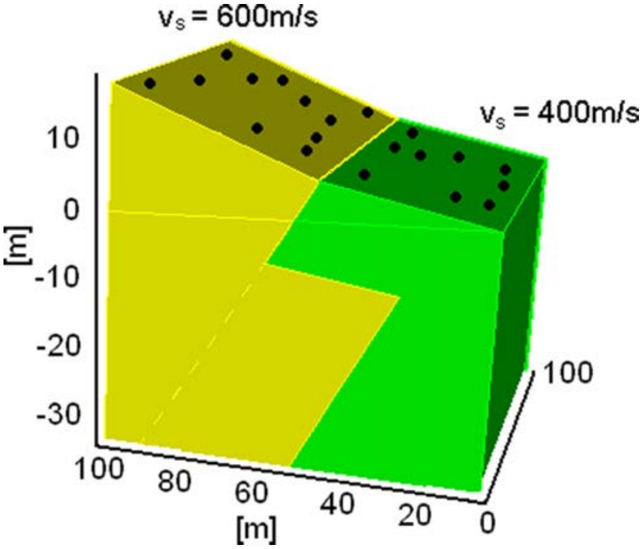

Figure 2. Simple 3-D structure used for the calculation of the noise synthetics. The two blocks are characterized by different shear-wave velocities. The black dots show the location of the receivers on the surface of the block.

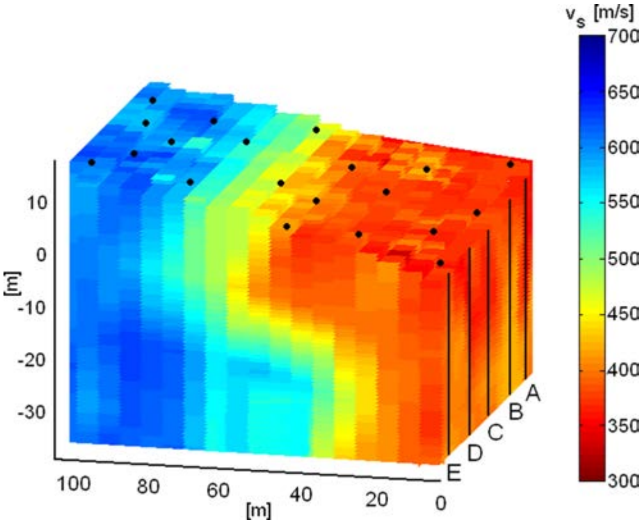

Figure 3. Inversion results for the model shown in Fig. 2 using noise synthetics. The images were obtained after 500 iterations. Black dots represent the receivers. Vertical black lines indicate cross-sections parallel to the topographic gradient for the resolution tests shown in Fig. 5.

From the continuous data sets recorded by 20 receivers, 60 noise windows of 30 s were extracted. Picozzi *et al.* (2009) have shown that this duration is sufficient for obtaining a reliable estimate of the Green's function between two sensors for distances of some tens of meters. After removing the linear trend from each window, a 5 per cent cosine taper was applied at both ends. For each frequency (5 Hz $\leq f \leq$ 15 Hz at intervals of 1 Hz) the traveltime between each pair of receivers has been calculated and the final inversion has been carried out using five different frequency values (5, 6, 9, 12 and 15 Hz).

In Fig. 3, the inversion results giving the average S-wave velocities are shown. The comparison between the input structure and the calculated velocities shows that the structure is satisfactorily reproduced. The two blocks characterized by different S-wave velocities and their shift for deeper parts of the block can clearly be identified. The absolute S-wave velocities are fairly well reproduced. However, since a set of smoothing parameters has been introduced in the solution, there is no sharp contrast between the two blocks, but only a more gradual transition. Nonetheless, we offer a note of caution: Since the resolution of our imaging technique is expected to decrease with depth, thus the tomographic signature of the velocity contrasts becomes weaker with increasing depth. Eq. (4) further implies that the vertical weights vary smoothly, from which it follows that vertical discontinuities and S-wave velocity inversions (i.e. a cell having an S-wave velocity lower than the corresponding cell above) will be resolved less sharply.

6 RESOLUTION TESTS

A meaningful and reliable interpretation of tomographic results requires an accurate analysis of the solution quality with all available resolution tools. To this regard, checkerboard resolution tests were carried out to confirm that the major velocity features can be

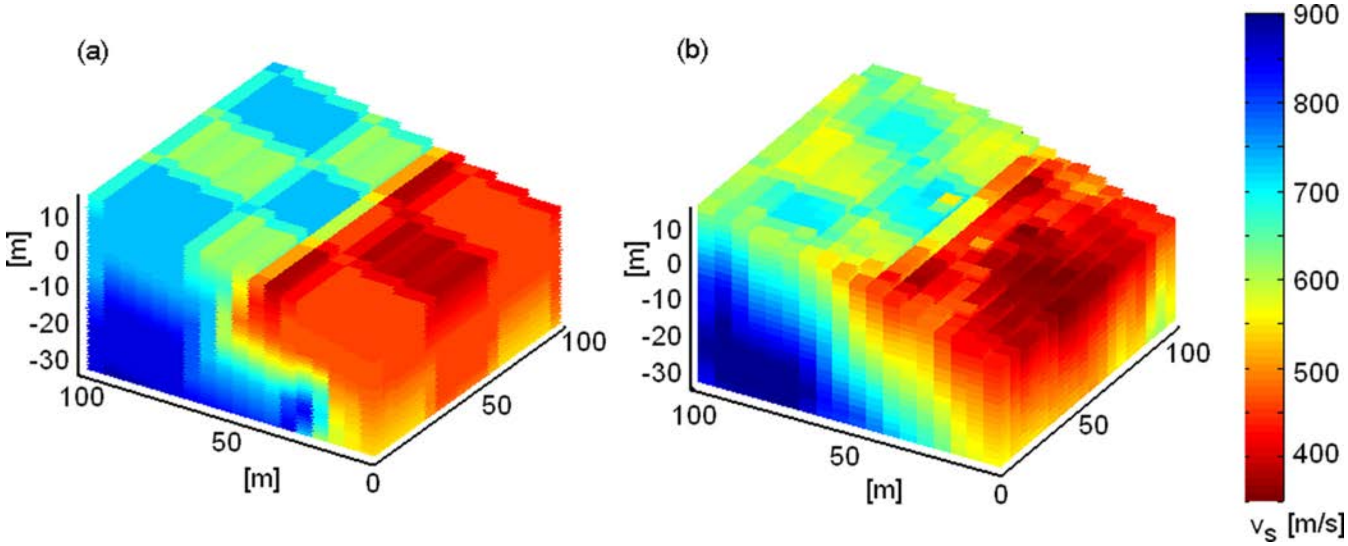

Figure 4. 3-D tomography with checkerboard. (a) The perturbed velocity model, generated by adding 20 per cent perturbation for every 20 m of depth below the surface on the initial model shown in Fig. 2. (b) The reconstructed model from the 3-D tomography.

adequately resolved. Our 3-D checkerboard test consists of adding a regularly varying perturbation with the appearance of a 3-D checkerboard to the final velocity model derived from the tomographic inversion. Based on the checkerboard, traveltimes are then calculated through the perturbed model, and a random traveltime variation is added to simulate realistic arrival times. The random times are selected from Gaussian distributions whose half-widths are consistent with the standard error estimates for the individual traveltime data (maximum error 0.007 s). Resolvability at any point of the model space is defined in terms of the ratio of recovered velocity anomaly to the real velocity perturbation.

The comparison between synthetic and restored models (Fig. 4) shows that both the checkerboard structure and the simulated anomaly are satisfactorily reproduced. A clear checkerboard structure can be identified on the top for the central area of the synthetic model where the path coverage is dense, giving a further strong indication that, in well resolved areas, the estimates of the recovered velocity anomalies are robust. Only at the edges of the model the ray coverage is insufficient to resolve the local structure with full confidence. In this case, the regularization acts to smooth the model towards lateral homogeneity. For the deepest parts, there is only limited recovery of the checkerboard due to the large decrease in the density of the rays with bottoming points, indicating poorer lateral resolution at depth. The near-surface properties are well resolved down to a depth of around 40 m.

For quantifying the resolution capacities of the proposed technique one can assess the quality of tomographic results by means of the full model resolution matrix which is routinely calculated in the inversion and which describes the distribution of information for each grid cell. The relative size and pattern of the off-diagonal elements of the resolution matrix show the way the information is smeared. For the velocity in a cell to be adequately resolved, its resolution should be peaked and should have no significant contribution from cells, which are adjacent. However, we base our analysis on the spread function (Michelini & McEvilly 1991), which has been found to be a better way for assessing the resolution than by solely examining the diagonal elements of the resolution matrix since the diagonal resolution is influenced by the grid size and the damping (Toomey & Foulger 1989). The spread function compresses each row of the model resolution matrix into a single number describing how strong and peaked the resolution is for that specific cell. Following Michelini & McEvilly (1991), the spread function S_j for a cell j can be computed from all elements r_{jk} of the corresponding row of the model resolution matrix $\mathbf{R}$ weighted by their distance d_{jk} from the node

$$S_j = \log\left[|r_j|^{-1}\sum_{k=1}^{M\cdot N}\left(\frac{r_{jk}}{|r_j|}\right)^2 d_{jk}\right] \qquad (5)$$

with the column index k for all M cells in each of the N horizontal layers, respectively. The elements of the resolution matrix in eq. (5) are normalized such that the sum of their squares is equal to one. $|r_j|$ is the L_2 norm and can be interpreted as a weighting factor that takes into account the value of the resolution kernel for each parameter. It follows from eq. (5) that in areas of high resolution the values of the spread function are small. However, as shown by Toomey & Foulger (1989), there is no universally applicable value to define the range of acceptable values of the spread function since the range of values obtained for the same data set will vary depending on the chosen damping and cell size.

In Fig. 5 the resolution of the velocity model shown in Fig. 3 is displayed by the spread function. It is clear that where there is adequate resolution the velocity reasonably agrees with the values of the underlying model. Overall the resolution close to the surface is high, in particular for the left part of cross-section E in Fig. 5. Similar to the horizontal weights also the horizontal model resolution of a cell depends on the number of rays crossing the cell and their angular distribution, rather than by the presence of nearby receivers, meaning that also the edges of the block show relatively high resolution except for the central part of cross-section A in Fig. 5.

There is a decrease in resolution with depth since fewer frequencies sample these parts of the block. The model can be well resolved down to a depth of around 35–40 m, being approximately one-third to one-half the wavelength of the lowest frequency. The depth might even be increased using more extended array configurations. Such depths cannot be reached by traditional methods such as trenching, pointing out the potential of the method for imaging near-surface structures.

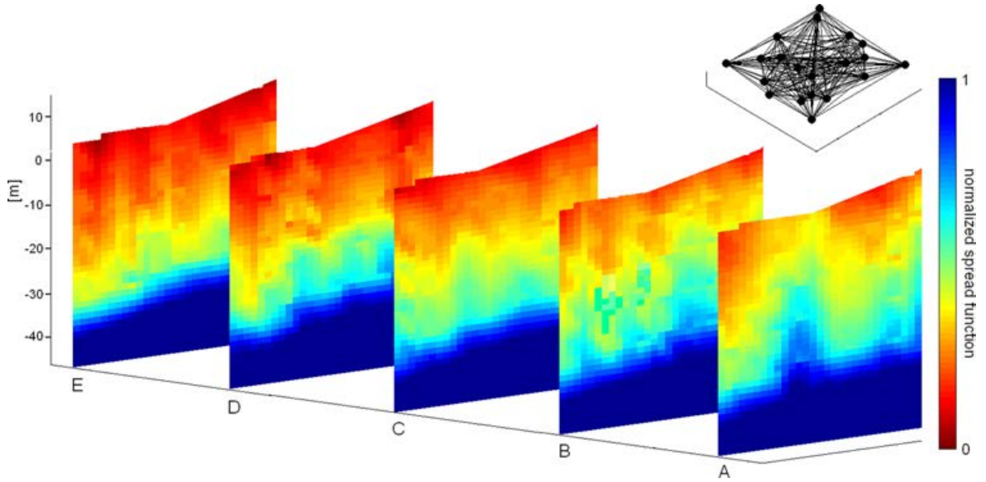

Figure 5. Horizontal cross-sections of the normalized spread function for the *S*-wave velocity model shown in Fig. 3. Black dots show location of sensors and black lines represent the ray paths.

7 THE ISSYK-ATA FAULT: CHARACTERISTICS AND DATA ACQUISITION

The studied natural example for obtaining images by means of real-world data is the Issyk-Ata fault in Kyrgyzstan, a moderately dipping thrust to reverse fault defining the northern deformation front for the central Tien Shan between $\sim$74°E and $\sim$75°E longitude (Fig. 6; Chediya *et al.* 1998; Thompson *et al.* 2002). Although the fault has not ruptured within the last 200 yr (and possibly longer) and has been believed to be seismically less active, traces of palaeoseismic deformations indicate that strong earthquakes have occurred in the past in this area and hence will probably occur again in the future (Abrakhmatov *et al.* 2002; Landgraf *et al.* 2012). A probabilistic assessment of the seismic hazard has recently been computed on a regional scale (Abrakhmatov *et al.* 2003; Erdik *et al.* 2005; Bindi *et al.* 2011) showing that the highest hazard for the country of Kyrgyzstan lies along the southern border of the city of Bishkek, the country's capital with almost one million inhabitants, close to the Issyk-Ata fault system. Thompson *et al.* (2002) have estimated a Quaternary slip rate of $2.1 + 1.7/{-0.3}$ mm yr^{-1} for the central part of the fault.

For our study, the data set is comprised of simultaneous recordings of seismic noise at 18 sites deployed in the Orto-Say district in southern Bishkek, spanning an area of 240 m × 160 m with the highest station being located around 20 m above the lowest and at the same time presumably crossing the surface appearance of the Issyk-Ata fault considering geological information (Chediya *et al.* 2000). In fact, although the precise location of the fault is hardly known some studies (e.g. Korjenkov *et al.* 2012) locate the fault near the base of the foothills limiting the Chuy basin to the south.

The array consisted of 14 Earth Data Logger (EDL) 24-bit acquisition systems equipped with 12 short-period Mark L4C-3D sensors, a Güralp CMG-ESPC 60 and a IO-3D 4.5 Hz sensor, and 4 Reftek 130 digitizers connected to Lennartz Le3D-5s seismometers. Seismic noise was recorded simultaneously by all stations for more than 2 hr on 2008 August 18 at a sampling rate of 500 samples s^{-1}. The continuous data sets were divided into 240 windows of 30 s. Following the same course of action as described in the previous paragraphs the SPAC coefficients and the corresponding traveltimes between all stations in a frequency range of $3\,\mathrm{Hz} \leq f \leq 13\,\mathrm{Hz}$ at intervals of 1 Hz have been calculated. The

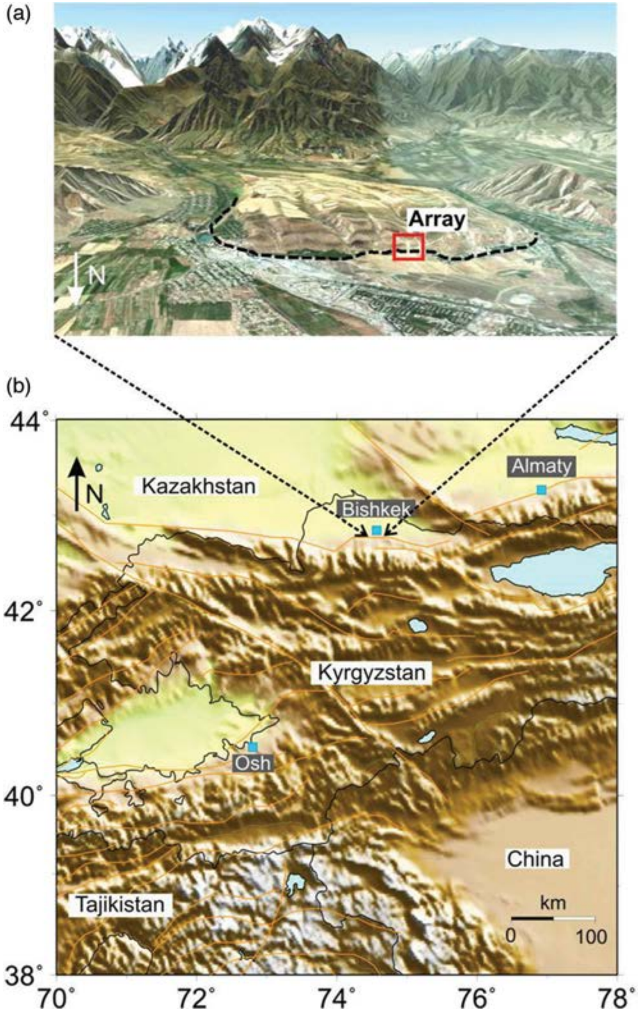

Figure 6. (a) Satellite image showing the southern outskirts of Bishkek facing the Ala-Too range. The topography is exaggerated by two times. Location of the array measurement is indicated. The dotted line shows the Issyk-Ata fault following Chediya *et al.* (2000). Google Earth, © 2012, CNS Spot Image © 2012, Digital Globe © 2012. (b) Map of Central Asia. Major faults are mapped in orange.

frequency–wavenumber (*f*–*k*) analysis carried out using the maximum likelihood method (Capon *et al.* 1967) shows that the anthropogenic seismic noise sources in this frequency range are more scattered over the wavenumber plane, with the largest energy coming from a narrow azimuthal range in the north being around 90° wide, that is, from the city of Bishkek (not shown). Although such a non-uniform distribution of seismic noise sources might bias the reconstruction of attenuation of the studied media when one-bit normalization is used (Larose *et al.* 2007) it will have only very minor influence on the phase, that is, on the calculation of the traveltimes, provided sufficiently long recording times in which enough energy is coming from the remaining azimuthal sectors (Derode *et al.* 2003; Larose *et al.* 2007; Yang & Ritzwoller 2008; Picozzi *et al.* 2009; Yao & van der Hilst 2009). Even if all the noise sources are distributed in an even narrow range the velocity error will be in the order of a few percent (Cupillard & Capdeville 2010), which can be tolerated in engineering seismology. Using 120 min of recording, the estimated traveltimes were found to be stable and have been inverted by a tomographic approach using five different frequency values (4, 5, 7, 10 and 13 Hz).

8 TOMOGRAPHIC IMAGING RESULTS AND INTERPRETATION

The inversion results of the array recordings obtained after 500 iterations are shown in Fig. 7. A clear difference in *S*-wave velocity is observed, contrasting the northern and the southern parts of the studied area and running in an east-west direction parallel to the fault. Such a rather strong velocity contrast across the Issyk-Ata fault close to the surface is not a unique feature and has already been observed for other faults (Lewis *et al.* 2007; Roux *et al.* 2011). The transition zone is rather sharp, spanning only some tens of meters. On such small scales of up to 10 m, representing the internal fault zone structure, regularization of geometrical incompatibilities on the fault surface with progressive slip produces a tabular zone of granular rock that becomes fault gouge. Based on Ben-Zion & Sammis (2003) and Korjenkov *et al.* (2012) we interpret this sharp velocity contrast as such a consistent fault structure tending to evolve with cumulative slip towards geometrical simplicity.

A distinct low-velocity wedge in the uppermost part of the northern section of the studied area can be identified (reddish colour in Figs 8a and b) which might be caused by fault scarp weathering and present-day detritus which had slid off from the rock terrace. In this interpretation, formation of the colluvial wedge would represent multiple faulting events with a total displacement of around 10 m; this value is similar to the findings of Korjenkov *et al.* (2012) who carried out geological investigations around 1 km to the east of our study site.

The estimated absolute *S*-wave velocities are robust and compatible with the findings of previous studies (Parolai *et al.* 2010) for similar material in Bishkek. Below the low-velocity deposits the material can be interpreted as late Pleistocene and Holocene terraces of boulder-pebble conglomerates and alluvial fans that form the lower surface of the alluvium plain of the Chu basin (Korjenkov *et al.* 2012). Of course, stratigraphy becomes more difficult to interpret northward due to the spatially and temporally discontinuous nature of deposition and erosion. On the contrary, Pliocene conglomerates with dense carbonate cement with gravel stones form the high velocity bluish part in the south (Korjenkov *et al.* 2012, Figs 8a and b). Whereas such clear differences can be found in the north–south cross-sections and might be interpreted as shallow fault traces for both east–west cross-sections, on the contrary, the velocity and most probably also the material is rather homogeneous with no lateral discontinuities (Figs 8c and d).

The dip angle of the fault close to the surface is around 50°. Although the exact dipping cannot completely be recovered due to intrinsic vertical smearing of the inversion algorithm the detected value is in agreement with Bullen *et al.* (2001) who is reporting dip angles in the range of 45°–50°. This information is valuable for the calculation of Quaternary shortening (Bullen *et al.* 2003) but it can also be used for the assessment of reliable seismic risk scenarios. It has been reported that the near-fault fault-normal peak velocities strongly depend on fault dip (e.g. Oglesby *et al.* 2000) and that for dipping angles greater than ∼50° the maximum fault-normal

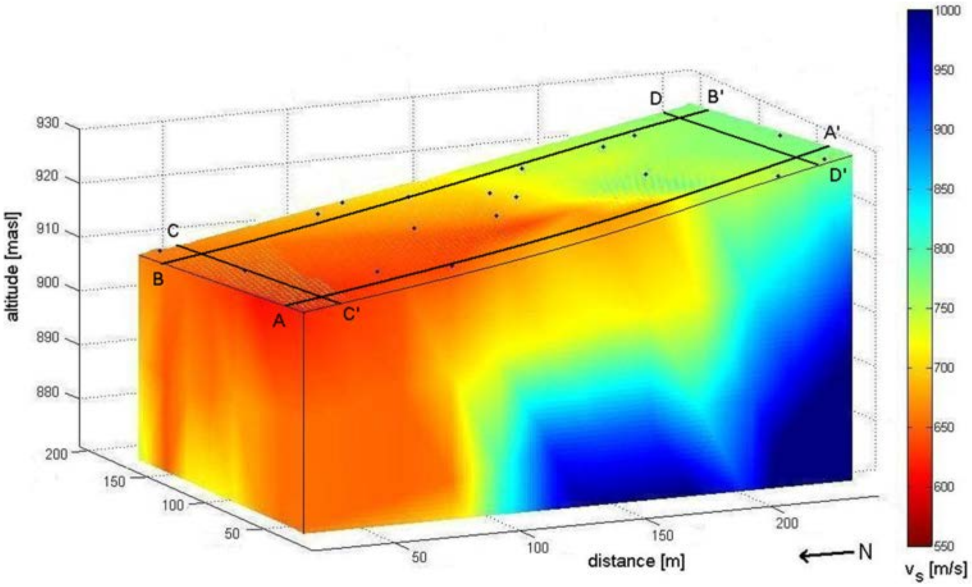

Figure 7. Inversion results of measurements on the Issyk-Ata fault obtained after 500 iterations. Topography is exaggerated about three times. The dots represent locations of the sensors. Locations of cross-sections shown in Fig. 8 are indicated by straight black lines.

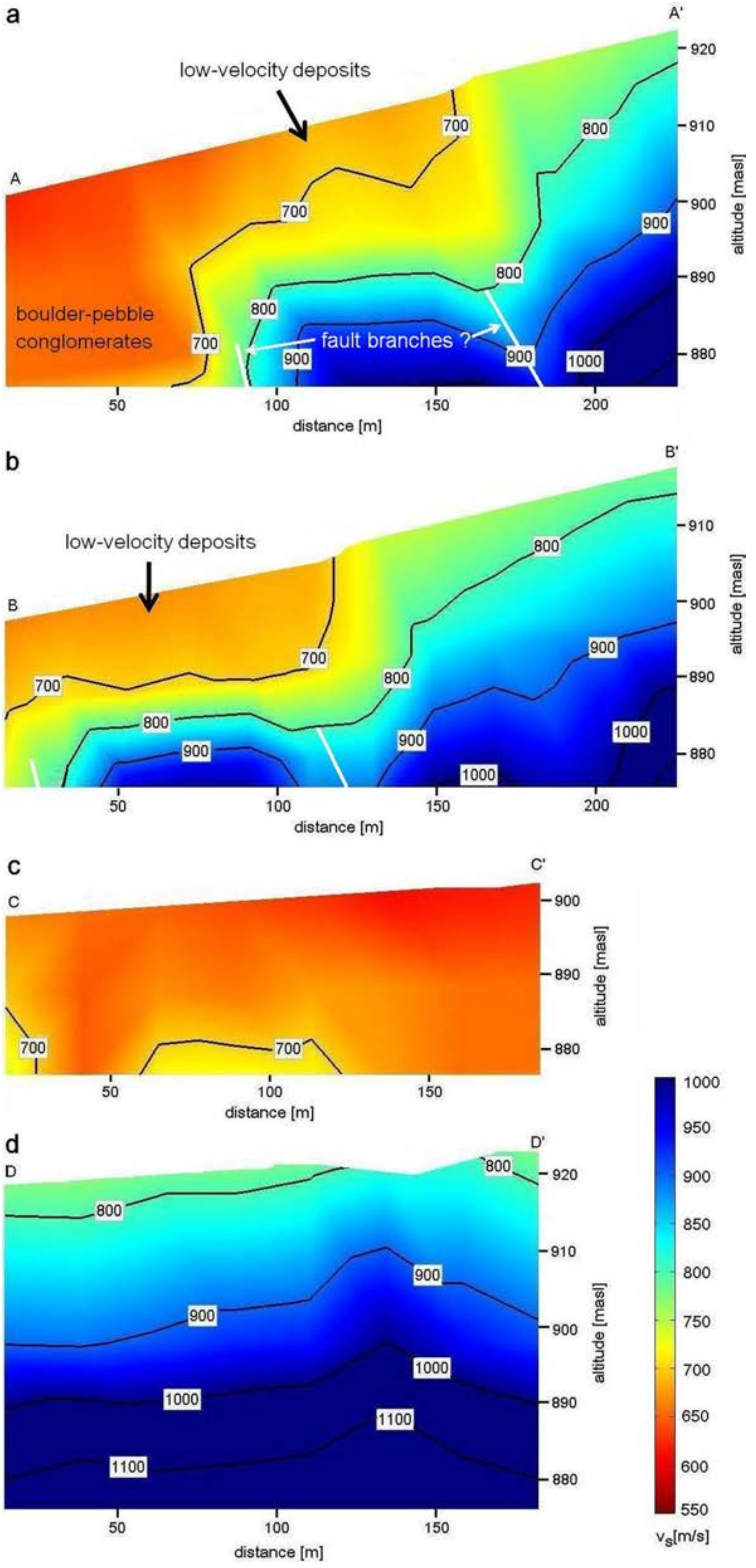

Figure 8. Cross-sections from the 3-D *S*-wave velocity model with (a) and (b) being north–south cross-sections and (c) and (d) being east–west cross-sections. For all profiles the topography is exaggerated about three times. Velocity isolines are mapped as thick black lines.

peak velocities will appear on the footwall (O'Connell *et al.* 2007), that is, north of the Issyk-Ata fault. Additionally, following Ma & Beroza (2008), the ground motion on the footwall might further be amplified due to the more compliant low velocity materials. Therefore, to obtain realistic estimates of ground motion it is therefore unavoidable to consider also the fault dip as well as the strong lateral velocity contrasts across the top several kilometres in ground motion prediction relations.

Two parallel fault structures can clearly be depicted (Figs 8a and b), one lowering the Tertiary by nearly 30 m, and the other lowering the top of the Tertiary strata to greater, but unresolved, depths to the north. Chediya *et al.* (2000) already found that the alluvial sequence in this fault zone can be disturbed by several thrusts that are generally concordant with the main fault. Also Korjenkov *et al.* (2012) elaborate the existence of such secondary splitting faults along the foothills in the same area. Such splitting effects could be the source of the high-frequency content of strong ground motion (Bhat *et al.* 2007), exposing the city of Bishkek to a high level of hazard.

9 OUTLOOK AND CONCLUSIONS

Based on the correlation of seismic noise recordings, we have shown that with a limited number of seismic stations and recording times of several tens of minutes, detailed images of the local subsoil structure can be obtained even under pronounced topographic conditions. The reliability of the proposed technique and its resolution capacity were validated using synthetic data sets showing that the results are well constrained. The displayed images obtained by synthetic data and for a real-world example, the Issyk-Ata fault in Kyrgyzstan, which may act as a major contributor of earthquake ground motion and basin-generated wave field effects in the Chu basin and the city of Bishkek, can serve as a valuable example that such images can be obtained even in cases of significant topography relief. In contrast to information gained from traditional 2-D trench excavation, such pointwise seismic imaging can add an extra dimension and a deeper perspective. In particular, the depth of investigation might be enlarged using more extended array configurations. Our study demonstrates that useful results in terms of realistic velocity structures and geometries can be obtained even in complex environments whose geology and physical properties are hardly known.

The speed of the urban growth with an increase in Bishkek's population of almost 10 per cent in the last 10 yr (Abdykalykov *et al.* 2009) is exposing more and more people and expanding infrastructures to seismic hazards. In combination with earthquake early warning and rapid response procedures for real-time risk assessment (Picozzi *et al.* 2013), several similar arrays distributed along the fault can be used for precise monitoring. In particular, making use of low cost and wireless self-organizing seismic sensors can serve as an alternative and new technique without the need for a planned, centralized infrastructure (Picozzi *et al.* 2010). The presented method can overcome shortcomings like poor spatial resolution which have been reported for other passive processing techniques in complex structures like volcanoes or fault zones (Sabra *et al.* 2006; Sens-Schönfelder & Wegler 2006; Wegler & Sens-Schönfelder 2007; Hadziioannou *et al.* 2009). While the classical SPAC equations have been derived for the analysis of the vertical component of ground motion they can in principle be adapted for the analysis of the horizontal components although the extraction of phase-velocity information for the single phases is not straightforward due to the superposition of both Rayleigh and Love waves (Boxberger *et al.* 2011). Anyhow, since the presented method only uses the phase and not the amplitude information associated with the direct or scattered waves, the scattered part of the correlation functions is stable enough to provide robust velocity estimates with which changes in the medium properties can be monitored.

Therefore, the method is particularly advantageous since it can return useful information about the heterogeneous subsurface structure and structural changes therein in complex environments across seismic faults or areas prone to landslides almost in real time even if earthquakes do not occur. Although such information about the *S*-wave velocity distribution is difficult to acquire with traditional methods, simply analysing the ambient noise field by the means described here can serve as a reliable and economical alternative.

ACKNOWLEDGEMENTS

Research has been carried out under the project MIIC – Monitoring and Imaging by Interferometric Concepts founded by the German Ministry of Education and Research (BMBF Project 03G0736B). We are grateful to U. Abdybachaev, P. Augliera, E. D'Alema, S. Orunbaev, A. Strollo, J. Tokmulin and S. Usupaev for assistance during the field work. K. Fleming kindly revised our English. Instruments were provided by the Geophysical Instrumental Pool of the Helmholtz Center Potsdam.

REFERENCES

Abdykalykov, O., Baijumanov, D., Osmonaliev, A., Tulegabylov, N., Kim, A., Koichumanova, K., Plesovskih, R. & Turdubaeva, Ch., 2009. Population and housing census of the Kyrgyz Republic of 2009, in *Main Social and Demographic Characteristics of Population and Number of Housing Units,* the National Statistical Committee of the Kyrgyz Republic, Bishkek, Kyrgyzstan.

Abrakhmatov, K., Delvaux, D. & Djanuzakov, K.D., 2002. Active tectonics and seismic hazard of the Issyk-Kul basin in the Kyrgyz Tien Shan, in *Lake Issyk-Kul: Its Natural Environment,* Vol. 13, *Earth and Environmental Sciences,* pp. 147–160, eds Klerx, J. & Imanackunov, B, NATO Science Series, Kluwer, The Netherlands.

Abrakhmatov, K., Havenith, H.B., Delvaux, D., Jongmans, D. & Trefois, P., 2003. Probabilistic PGA and Arias Intensity Maps of Kyrgyzstan (Central Asia), *J. Seismol.,* **7,** 203–220.

Aki, K., 1957. Space and time spectra of stationary stochastic waves with special reference to microtremors, *Bull. Earthq. Res. Inst. Tokyo Univ.,* **35,** 415–456.

Aki, K. & Lee, W.H.K., 1976. Determination of three-dimensional velocity anomalies under a seismic array using first P arrival times from local earthquakes, 1: a homogeneous initial model, *J. geophys. Res.,* **81,** 4381–4399.

Aki, K. & Richards, P.G., 1980. *Quantitative Sesimology: Theory and Methods,* Vol. II, W. H. Freeman and Company, San Francisco, USA.

Amato, A., Chiarabba, C., Malagnini, L. & Selvaggi, G., 1992. Three-dimensional P-velocity structure in the region of the Ms = 6.9 Irpinia, Italy, normal faulting earthquake, *Phys. Earth planet. Int.,* **75,** 111–119.

Ammon, C.J. & Vidale, J.E., 1993. Tomography without rays, *Bull. seism. Soc. Am.,* **83,** 509–528.

Arai, H. & Tokimatsu, K., 2004. S-wave velocity profiling by inversion of microtremor H/V spectrum, *Bull. seism. Soc. Am.,* **94,** 53–63.

Ben-Zion, Y., 1989. The response of two joined quarter spaces to SH line sources located at the material discontinuity interface, *Geophys. J. Int.,* **98,** 213–222.

Ben-Zion, Y. & Malin, P., 1991. San Andreas fault zone head waves near Parkfield, California, *Science,* **251,** 1592–1594.

Ben-Zion, Y. & Sammis, C.G., 2003. Characterization of fault zones, *Pure appl. Geophys.,* **160,** 677–715.

Ben-Zion, Y. & Shi, Z.Q., 2005. Dynamic rupture on a material interface with spontaneous generation of plastic strain in the bulk, *Earth planet. Sci. Lett.,* **236,** 486–496.

Bhat, H.S., Olives, M., Dmowska, R. & Rice, J.R., 2007. Role of fault branches in earthquake rupture dynamics, *J. geophys. Res.,* **112,** B11309, doi:10.1029/2007JB005027.

Bindi, D., Mayfield, M., Parolai, S., Tyagunov, S., Begaliev, U.T., Abdrakhmatov, K., Moldobekov, B. & Zschau, J., 2011. Towards an improved seismic risk scenario for Bishkek, Kyrgyz Republic, *Soil Dyn. Earthq. Eng.,* **31,** 521–525.

Boxberger, T., Picozzi, M. & Parolai, S., 2011. Shallow geology charactirization using raleigh and love wave dispersion curves derived from seismic noise array measurements, *J. appl. Geophys.*, **75,** 345–354.

Brenguier, F., Shapiro, N.M., Campillo, M., Nercessian, A. & Ferrazzini, V., 2007. 3-D surface wave tomography of the Piton de la Fournaise volcano using seismic noise correlations, *Geophys. Res. Lett.*, **34,** L02305, doi:10.1029/2006GL028586.

Bullen, K.E., 1963. *An introduction to the theory of seismology,* Cambridge University Press, Cambridge.

Bullen, M.E., Burbank, D.W., Garver, J.I. & Abdrakhmatov, K.Y., 2001. Late Cenozoic tectonic evolution of the northwestern Tien Shan: new age estimates for the initiation of mountain building, *Geol. Soc. Am. Bull.*, **113,** 1544–1559.

Bullen, M.E., Burbank, D.W. & Garver, J.I., 2003. Building the northern Tien Shan: integrated thermal, structural, and topographic constraints, *J. Geol.*, **111,** 149–165.

Campillo, M. & Paul, A., 2003. Long-range correlations in the diffuse seismic coda, *Science,* **299,** 547–549.

Capon, J., Greenfield, R.J. & Kolker, R.J., 1967. Multidimensional maximum-likelihood processing of a large aperture seismic array, *Proc. IEEE,* **55,** 192–211.

Cattaneo, M. & Eva, C., 1990. Propagation anomalies in northwestern Italy by inversion of teleseismic residuals, *Terra Nova,* **2,** 577–584.

Chediya, O.K., Abdrakhmatov, K.Y., Lemzin, I.H., Mihel, G. & Mikhailev, V., 1998. *Seismotectonic characterization of the Issyk Ata fault,* Naukai Novye Technologii, Bishkek, Kyrgyzstan, pp. 58–69.

Chediya, O.K., Abdrakhmatov, K.Y., Lemzin, I.H., Mihel, G. & Mikhailev, V., 2000. Issyk Ata, North Tien Shan fault in the Holocene, *J. Earthq. Pred. Res.*, **8,** 379–386.

Cupillard, P. & Capdeville, Y., 2010. On the amplitude of surface waves obtained by noise correlation and the capability to recover the attenuation: a numerical approach, *Geophys. J. Int.*, **181,** 1687–1700.

Derode, A., Larose, E., Tanter, M., de Rosny, J., Tourin, A., Campillo, M. & Fink, M., 2003. Recovering the Green's function from field-field correlations in an open scattering medium, *J. acoust. Soc. Am.,* **113,** 2973–2976.

Dor, O., Yildirim, C., Rockwell, T.K., Ben-Zion, Y., Emre, O., Sisk, M. & Duman, T.Y., 2008. Geologic and geomorphologic asymmetry across the rupture zones of the 1943 and 1944 earthquakes on the North Anatolian Fault: possible signals for preferred earthquake propagation direction, *Geophys. J. Int.*, **173,** 483–504.

Eberhart-Phillips, D. & Michael, A.J., 1993. Three-dimensional velocity, structure, seismicity, and fault structure in the Parkfield region, Central California, *J. geophys. Res.*, **98,** 15 737–15 757.

Ekström, G., Abers, G.A. & Webb, S.C., 2009. Determination of surface-wave phase velocities across USArray from noise and Aki's spectral formulation, *Geophys. Res. Lett.,* **36,** L18301, doi:10.1029/2009GL039131.

Erdik, M., Rashidov, T., Safak, E. & Turdukulov, A., 2005. Assessment of seismic risk in Tashkent, Uzbekistan and Bishkek, Kyrgyz Republic, *Soil Dyn. Earthq. Eng.,* **25,** 473–486.

Evans, J.R. & Achauer, U., 1993. Teleseismic velocity tomography using the ACH method: theory and application to continental-scale studies, in *Seismic Tomography: Theory and Practice,* eds Iyer, H.M. & Hirahara, K., Chapman and Hall, London.

Faccioli, E., Maggio, F., Paolucci, R. & Quarteroni, A., 1997. 2D and 3D elastic wave propagation by a pseudo-spectral domain decomposition method, *J. Seismol.,* **1,** 237–251.

Foti, S., Comina, C., Boiero, D. & Socco, L.V., 2009. Non uniqueness in surface wave inversion and consequences on seismic site response analyses, *Soil Dyn. Earthq. Eng.,* **29,** 982–993.

Foti, S., Parolai, S., Albarello, D. & Picozzi, M., 2011. Application of surface-wave methods for seismic site characterization, *Surv. Geophys.,* **32,** 777–825.

Hadziioannou, C., Larose, E., Coutant, O., Roux, P. & Campillo, M., 2009. Stability of monitoring weak changes in multiply scattering media with ambient noise correlation: laboratory experiments, *J. acoust. Soc. Am.,* **125,** 3688–3695.

Heaton, H.T. & Heaton, R.E., 1989. Static deformation from point forces and force couples located in welded elastic Poissonian half-spaces: implications for seismic moment tensors, *Bull. seism. Soc. Am.,* **79,** 813–841.

Kissling, E., 1988. Geotomography with local earthquake data, *Rev. Geophys.,* **25,** 659–698.

Korjenkov, A.M., Kolchenko, V.A., Rott, P.G. & Abdieva, S.V., 2012. Strong mediaeval earthquakes in the Chuy basin, Kyrgyzstan, *Geotectonics,* **46,** 303–314.

Kugler, S., Bohlen, T., Forbriger, T., Bussat, S. & Klein, G., 2007. Scholte-wave tomography for shallow-water marine sediments, *Geophys. J. Int.,* **168,** 551–570.

Lachet, C. & Bard, P.Y., 1994. Numerical and theoretical investigations on the possibilities and limitations of Nakamura's technique, *J. Phys. Earth,* **42,** 377–397.

Landgraf, A., Abrakhmatov, K., Djumabaeva, A., Strecker, M.R. & Arrowsmith, R., 2012. Paleoseismological investigations along a newly developing fault in the northern Tien Shan foreland near Bishkek, Kyrgyzstan, in *Proceedings of the International Workshop on Active Tectonics, Paleoseismology and Archaeoseismology,* Morelia, Mexico, SF 1.1.2.

Larose, E., Roux, P. & Campillo, M., 2007. Reconstruction of Rayleigh-Lamb dispersion spectrum based on noise obtained from an air-jet forcing, *J. acoust. Soc. Am.,* **122,** 3437–3444.

Lay, T. & Wallace, T.C., 1995. *Modern Global Seismology,* Academic Press, San Diego.

Lewis, M.A., Ben-Zion, Y. & McGuire, J., 2007. Imaging the deep structure of the San Andreas Fault south of Hollister with joint analysis of fault-zone head and direct P arrivals, *Geophys. J. Int.,* **169,** 1028–1042.

Ma, S. & Beroza, G.C., 2008. Rupture dynamics on a bimaterial interface for dipping faults, *Bull. seism. Soc. Am.,* **98,** 1642–1658.

McNally, K.C. & McEvilly, T.V., 1977. Velocity contrast across the San Andreas Fault in central California, small-scale variations from P-wave nodal plane distortion, *Bull. seism. Soc. Am.,* **67,** 1565–1576.

Michelini, A. & McEvilly, T.V., 1991. Seismological studies at Parkfield, I. Simultaneous inversion for velocity structure and hypocenters using cubic B-spline parameterization, *Bull. seism. Soc. Am.,* **81,** 524–552.

Mitchell, T.M., Ben-Zion, Y. & Shimamoto, T., 2011. Pulverized fault rocks and damage asymmetry along the Arima-Takatsuki Tectonic Line, Japan, *Earth planet. Sci. Lett.,* **308,** 284–297.

Mooney, W.D., 1989. Seismic methods for determining earthquake source parameters and lithospheric structure, in *Geophysical Framework of the Continental United States,* Mem. Geol. Soc. Am. 172, pp. 11–34, eds Pakiser, L.C. & Mooney, W.D., The Geological Society of America, Boulder, CO.

Mooney, W.D. & Brocher, T.M., 1987. Coincident seismic reflection/refraction studies of the continental lithosphere: a global review, *Rev. Geophys.,* **25,** 723–774.

O'Connell, D.R.H., Ma, S. & Archuleta, R.J., 2007. Influence of dip and velocity heterogeneity on reverse- and normal-faulting rupture dynamics and near-fault ground motions, *Bull. seism. Soc. Am.,* **97,** 1970–1989.

Oglesby, D.D., Archuleta, R.J. & Nielsen, S.B., 2000. The three-dimensional dynamics of dipping faults, *Bull. seism. Soc. Am.,* **90,** 616–628.

Ohori, M., Nobata, A. & Wakamatsu, K., 2002. A comparison of ESAC and FK methods of estimating phase velocity using arbitrarily shaped microtremor arrays, *Bull. seism. Soc. Am.,* **96,** 2323–2332.

Oppenheimer, D.H., Reasenberg, P.A. & Simpson, R.W., 1988. Fault plane solutions for the 1984 Morgan Hill, California, earthquake sequence: evidence for the state of stress on the Calaveras fault, *J. geophys. Res.,* **93,** 9007–9026.

Parolai, S. *et al.*, 2010. Site effects assessment in Bishkek (Kyrgyzstan) using earthquake and noise recording data, *Bull. seism. Soc. Am.,* **100,** 3068–3082.

Perton, M., Sánchez-Sesma, F.J., Rodríguez-Castellanos, A., Campillo, M. & Weaver, R., 2009. Two perspectives on equipartition in diffuse elastic fields in three dimensions, *J. acoust. Soc. Am.,* **126,** 1125–1130.

Picozzi, M., Parolai, S., Bindi, D. & Strollo, A., 2009. Characterization of shallow geology by high-frequency seismic noise tomography, *Geophys. J. Int.,* **176,** 164–174.

Picozzi, M., Milkereit, C., Parolai, S., Jaeckel, K.H., Veit, I., Fischer, J. & Zschau, J., 2010. GFZ wireless seismic array (GFZ-WISE), a wireless mesh network of seismic sensors: new perspectives for seismic noise array investigations and site monitoring, *Sensors,* **10,** 3280–3304.

Picozzi, M., Bindi, D., Pittore, M., Kieling, K. & Parolai, S., 2013. Real-time risk assessment in seismic early warning and rapid response: a feasibility study in Bishkek (Kyrgyzstan), *J. Seismol.,* **17,** 485–505.

Pilz, M., Parolai, S., Picozzi, M. & Bindi, D., 2012. Three-dimensional shear wave velocity imaging by ambient seismic noise tomography, *Geophys. J. Int.,* **189,** 501–512.

Roux, P., Wathelet, M. & Roueff, A., 2011. The San Andreas Fault revisited through seismic-noise and surface-wave tomography, *Geophys. Res. Lett.,* **38,** L13319, doi:10.1029/2011GL047811.

Sabra, K.G., Roux, P., Gerstoft, P., Kuperman, W.A. & Fehler, M.C., 2006. Extracting coda arrivals from cross-correlations of long period scattered waves during the Mount St. Helens 2004 eruption, *Geophys. Res. Lett.,* **33,** L06313.

Sánchez-Sesma, F.J., Pérez-Ruiz, J.A., Luzón, F., Campillo, M. & Rodriguez-Castellanos, A., 2008. Diffuse fields in dynamic elasticity, *Wave Motion,* **45,** 641–654.

Sánchez-Sesma, F.J. *et al.*, 2011. A theory for microtremor H/V spectral ratio: application for a layered medium, *Geophys. J. Int.,* **186,** 221–225.

Sengor, A.M.C., Tuysuz, O., Imren, C., Sakınc, M., Eyidogan, H., Gorur, N., Le Pichon, X. & Rangin, C., 2005. The north anatolian fault: a new look, *Ann. Rev. Earth planet. Sci.,* **33,** 37–112.

Sens-Schönfelder, C. & Wegler, U., 2006. Passive image interferometry and seasonal variations of seismic velocity at Merapi Volcano, Indonesia, *Geophys. Res. Lett.,* **33,** L21302, doi:10.1029/2006GL027797.

Thompson, S.C., Weldon, R.J., Rubin, C.M., Abdrakhmatov, K.Y., Molnar, P. & Berger, G.W., 2002. Late Quaternary slip rates across the central Tien Shan, Kyrgyzstan, central Asia, *J. geophys. Res.,* **107,** doi:10.1029/2001JB000596.

Toomey, D.R. & Foulger, G.R., 1989. Tomographic inversion of local earthquake data from the Hengill-Grensdalur central volcano complex, Iceland, *J. geophys. Res.,* **94,** 17 497–17 510.

Tsai, V. & Moschetti, M., 2010. An explicit relationship between time-domain noise correlation and spatial autocorrelation (SPAC) results, *Geophys. J. Int.,* **182,** 454–460.

Tukey, J.E., 1974. Introduction to today's data analysis, in *Proceedings of the Conference on Critical Evaluation of Chemical and Physical Structural Information*, pp. 3–14, eds Lide, D.R. & Paul, M.A., National Academy of Sciences, Washington, DC.

Wang, L., Luo, Y. & Xu, Y., 2012. Numerical investigation of Rayleigh-wave propagation on topography surface, *J. appl. Geophys.,* **86,** 88–97.

Wegler, U. & Sens-Schönfelder, C., 2007. Fault zone monitoring with passive image interferometry, *Geophys. J. Int.,* **168,** 1029–1033.

Xia, J., Miller, R.D. & Park, C.B., 1999. Estimation of near-surface shear-wave velocity by inversion of Rayleigh wave, *Geophysics,* **64,** 691–700.

Yang, Y. & Ritzwoller, M.H., 2008. Characteristics of ambient seismic noise as a source for surface wave tomography, *Geochem. Geophys. Geosyst.,* **9,** doi:10.1029/2007GC001814.

Yanovskaya, T.B. & Ditmar, P.G., 1990. Smoothness criteria in surface wave tomography, *Geophys. J. Int.,* **102,** 63–72.

Yao, H. & van der Hilst, R., 2009. Analysis of ambient noise energy distribution and phase velocity bias in ambient noise tomography with application to SE Tibet, *Geophys. J. Int.,* **179,** 1113–1132.